

Nonlinear Transient Survival Level Seismic Finite Element Analysis of Magellan Ground Based Telescope

Matt Griebel¹, Christine Buleri¹, Andrew Baylor¹, Steve Gunnels², Charlie Hull³, Povilas Palunas⁴, Mark Phillips⁴

¹Quartus Engineering, 10251 Vista Sorrento Parkway Suite 250, San Diego, CA, USA 92121; ²Paragon Engineering, 2277 Joy Lane, Westcliffe, CO, USA 81252; ³Carnegie Observatories, 813 Santa Barbara Street, Pasadena, CA, USA 91101; ⁴Las Campanas Observatory, Carnegie Institution of Washington, Colina El Pino Casilla 601 La Serena, Chile

ABSTRACT

The Magellan Telescopes are a set of twin 6.5 meter ground based optical/near-IR telescopes operated by the Carnegie Institution for Science at the Las Campanas Observatory (LCO) in Chile. The primary mirrors are $f/1.25$ paraboloids made of borosilicate glass and a honeycomb structure. The secondary mirror provides both $f/11$ and $f/5$ focal lengths with two Nasmyth, three auxiliary, and a Cassegrain port on the optical support structure (OSS).

The telescopes have been in operation since 2000 and have experienced several small earthquakes with no damage. Measurement of *in situ* response of the telescopes to seismic events showed significant dynamic amplification, however, the response of the telescopes to a survival level earthquake, including component level forces, displacements, accelerations, and stresses were unknown. The telescopes are supported with hydrostatic bearings that can lift up under high seismic loading, thus causing a nonlinear response. For this reason, the typical response spectrum analysis performed to analyze a survival level seismic earthquake is not sufficient in determining the true response of the structure. Therefore, a nonlinear transient finite element analysis (FEA) of the telescope structure was performed to assess high risk areas and develop acceleration responses for future instrument design. Several configurations were considered combining different installed components and altitude pointing directions. A description of the models, methodology, and results are presented.

Keywords: Magellan Telescopes, FEA, SLE, SLS, Abaqus, Direct Transient, Implicit Dynamic

1 INTRODUCTION

The Magellan Telescopes are a pair of 6.5 meter altitude-azimuth telescopes designed primarily for optical and near-infrared wavelengths. The primary mirror is an $f/1.25$ paraboloid. The telescope can provide both $f/11$ and $f/5$ secondary mirrors, with support for wide field view using a turret mounted tertiary mirror with atmospheric dispersion compensation (ADC). The telescopes were designed with instrumentation as a primary consideration, as well as to minimize image distortion due to thermal effects. Instrumentation is available at two Nasmyth locations, three auxiliary ports, and at the Cassegrain location on the optical support structure (OSS). Figure 1 shows the general layout of the Magellan Telescopes.

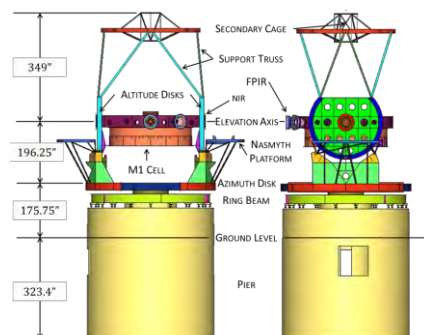


Figure 1 – Magellan Telescope structure and components

Las Campanas Observatory (LCO) is located in the southern Atacama Desert of Chile and is owned and operated by the Carnegie Institution for Science. LCO is home to many telescopes including the Magellan Telescopes, and is the future site of the Giant Magellan Telescope, a planned extremely large telescope with expected completion in 2021. With increasing seismic activity in Chile and at LCO, an in depth analysis of the Magellan Telescopes response to a survival level earthquake was necessary. Typically, sufficient information can be gleaned from a response spectrum analysis of the telescope. However, the Magellan Telescopes exhibit some nonlinearity that precludes the use of linear, frequency based analyses.

The telescopes are supported by hydrostatic bearings. The bearings are designed such that they only react compression forces. If a force exceeding the preload due to gravity is exerted on the bearing, it will experience lift off due to zero stiffness in tension. In addition, the secondary cage is positioned using actuators on the ends of the vanes. These vane end actuators are preloaded to maintain the relative position of the secondary mirror. These nonlinearities present some novel modeling and analysis complexities addressed in Section 2.

2 METHODOLOGY

A nonlinear transient survival level seismic finite element analysis of the Magellan Telescopes was performed using Abaqus/Standard 6.14-3 [1]. The two telescopes (Baade and Clay) are similar, but not identical. Two finite element models were created (approximately representing Baade and Clay, but with some variation to obtain additional information for use in possible future configurations). An implicit dynamic analysis was performed using a three-axis acceleration time history of a survival level earthquake as specified in the GMT Site-Specific Seismic Hazard Assessment created by URS Corporation in 2011 [2]. Although this report was generated for the GMT site, it was assumed valid for the nearby Magellan Telescope site as well. This report included several different time histories for survival level earthquakes that all produce the same shock response spectra. One was chosen due to its shorter duration while maintaining the same acceleration magnitudes compared to the others (Section 2.2). The specific rock stiffness underlying the Magellan Telescopes was calculated by Simpson, Gumpertz & Heger, Inc (SGH) and included in this analysis as described in Section 2.1 [3].

2.1 Finite element models

Two finite element models were created for the Magellan Telescopes in Hypermesh 13.0 [4]. One model (Configuration 1) more closely represents the configuration of the Baade Telescope, while the other (Configuration 2) represents the Clay Telescope. Both models are not exact representations of their respective parent telescopes, but are a close approximation of typical or expected secondary, tertiary, and auxiliary components. Table 1 lists the various components modeled in each configuration and Figure 2 shows their locations. One major difference is the stiffness of the primary mirror (M1) static supports. The M1 mirrors on the Magellan Telescopes are supported under larger displacements by a constellation of wire rope isolators. The FEM represents these as discrete connectors at each wire rope location with linear stiffness according to [5].

Table 2 lists the material properties used. The M1 mirror is a complicated structure that warrants its own analysis; therefore it was simply represented in this model. Three concentric rings were constructed and assigned the values listed in order to approximate its weight and stiffness. This approximation is not intended for a detailed stress analysis.

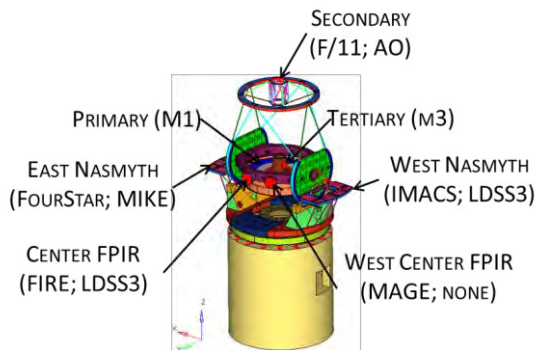


Figure 2 – Component locations for Configuration 1 and Configuration 2

Table 1 - Components modeled in each configuration. Total weight includes weight of structure and components not shown here.

Component	Configuration 1 Component	Comments	Configuration 2 Component	Comments
Primary Support	“Mag I”	22.85 lb/mm lat 39.17 lb/mm axi	“Mag II”	37.09 lb/mm lat 62.7 lb/mm axi
Secondary	f/11	800 lb	Adaptive Optics (AO)	1000 lb
Tertiary	M3 & ADC	750 lb (M3) 540 lb (ADC) 1,472 lb (turret)	M3	800 lb (M3) 1,973 (turret)
West Nasmyth Platform/ Nasmyth Instrument Rotator (NIR)	Inamori-Magellan Areal Camera & Spectrograph (IMACS)	7,700 lb	Low Dispersion Survey Spectrograph (LDSS3) – NIR Only	1,200 lb
East Nasmyth Platform/NIR	FourStar	2,100 lb	Magellan Inamori Kyocera Echelle (MIKE)	1,300 lb
Center Folded Port Instrument Rotator (FPIR)	Folded Port Infrared Echellette (FIRE)	1,500 lb	LDSS3	1,200 lb
West/Center FPIR	Magellan Echellette (MAGE)	700 lb	None	-
Total Weight (no pier)	-	406,850 lb	-	397, 240 lb
Total Weight (incl. pier)	-	3,047,299 lb	-	3,037,689 lb

Table 2 – Material properties

Material	Density (slinch/in ³)	Modulus (psi)	Poisson’s	Fty (ksi)	Ftu (ksi)
A36 Steel	7.35E-4	2.90E+7	0.26	36.3	58
1018 CR Steel	7.35E-4	2.90E+7	0.29	45	65.3
AISI 4130 Steel	7.324E-4	2.90E+7	0.32	70	90
6061-T6 Al	2.536E-4	9.90E+6	0.33	35	42
Reinforced Concrete	2.588E-4	5.00E+6	0.13	-	-
M1 Mirror Inner	2.36E-5	2.40E+5	0.2	-	-
M1 Mirror Middle	2.36E-5	2.59E+5	0.199	-	-
M1 Mirror Outer	2.36E-5	2.88E+5	0.196	-	-

Configuration 1 and Configuration 2 consist of linear reduced integration shell elements, linear hexahedral elements, linear beam elements, infinitely rigid kinematic and distributing couplings, and linear and nonlinear connector elements. Instruments were modeled with concentrated masses and rotary inertias (where appropriate) at their respective centers of gravity. Nonstructural mass (NSM) was added to the models to account for components not explicitly modeled including fasteners, wiring, staircases, etc. The OSS in each model was balanced about the azimuth and zenith axes by placing additional NSM at specified balancing locations used *in situ*. The models contain approximately 134,000 nodes and 129,000 elements each and weigh approximately 3.05 million lbs (the pier alone weighs approximately 2.64 million lbs). Figure 3 shows an overview of the Configuration 1 and some relative element mesh densities.

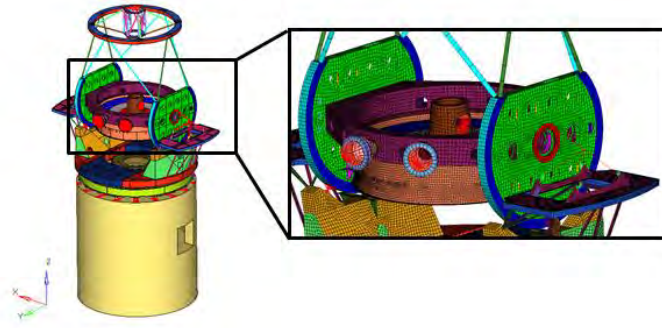


Figure 3 – Finite element model of Configuration 1 Magellan Telescope

The eighteen hydrostatic bearings (4 OSS Lateral, 4 OSS Radial, 4 Azimuth Radial, and 6 Azimuth Vertical) were modeled using connector elements. For this analysis, the OSS Lateral and Azimuth Radial bearings were assumed to have a linear response. The OSS Radial and Azimuth vertical were given nonlinear stiffness. Varying stiffnesses were used for each bearing based on bearing size and contact area. The nonlinear bearings exhibit only compression stiffness (zero stiffness in tension to allow lift off after force exceeds preload due to gravity). Each connector element has six degrees of freedom (DOF). Only the axial DOF was prescribed stiffness. All other DOF were given a small linear stiffness to aid convergence.

The 10 hydrostatic bearings with a component in the vertical direction (4 OSS Radial and 6 Azimuth Vertical) were also given friction in the lateral direction ($\mu = 0.1$), where frictional force is proportional to normal force.

The secondary vanes use actuators to adjust the position of the secondary mirror. In the zenith configuration, four radial actuators apply a radial preload of approximately 10,000 lbs. In the FEM, this was accomplished by applying a preload to a connector with no stiffness. The change in length required to develop the preload in zenith was applied to the Z60 configuration to maintain the same relative position (see Section 2.4 for configurations). The vanes developed appropriate preload based on the kinematic configuration of the system. As the acceleration time history was applied, the length of these vane end connectors was maintained, allowing them to take more or less load as determined by the stiffness of the model. In Configuration 1, the FourStar instrument also uses a preloaded beam connected to the Nasmyth platform so that the NIR only takes 20% of the weight of FourStar.

The telescopes are embedded in the ground with the pier structure (shown in pale yellow in Figure 3). In order to accurately model the telescope response, the soil was analyzed and a 6x6 DOF matrix was created as specified by SGH, Inc in *Foundation Stiffness for Seismic Analysis of Magellan Telescopes- 11 September 2015.pptx* [3]. Three stiffnesses were provided that enveloped the soil response (“stiff”, “soft”, and a mean response). This analysis used the “soft” response to be more conservative. Figure 4 shows the assembled stiffness matrix. K_h is horizontal stiffness, K_v is vertical stiffness, K_r is rotational stiffness, K_t is torsional stiffness, and K_{hr} are the coupled horizontal rotational stiffnesses. A connector was used between the pier and ground that allowed 36 DOF definitions to completely capture the soil response. The free end of the soil connector was used as the input for the time history of the seismic event.

$$\begin{vmatrix} K_h & 0 & 0 & 0 & K_{hr} & 0 \\ 0 & K_h & 0 & -K_{hr} & 0 & 0 \\ 0 & 0 & K_v & 0 & 0 & 0 \\ 0 & -K_{hr} & 0 & K_r & 0 & 0 \\ K_{hr} & 0 & 0 & 0 & K_r & 0 \\ 0 & 0 & 0 & 0 & 0 & K_t \end{vmatrix}$$

Figure 4 – 6x6 DOF Stiffness Matrix representing soil at Magellan site.

2.2 Survival level earthquake

Previous structural analyses of telescopes have shown that significant dynamic amplifications may occur during seismic events. The dynamic responses of the Magellan telescopes to a seismic event were unknown. Accelerometers were placed at critical locations on the telescope structure and accelerations were recorded during a minor seismic event. The accelerometers showed significant dynamic amplification (Figure 5).

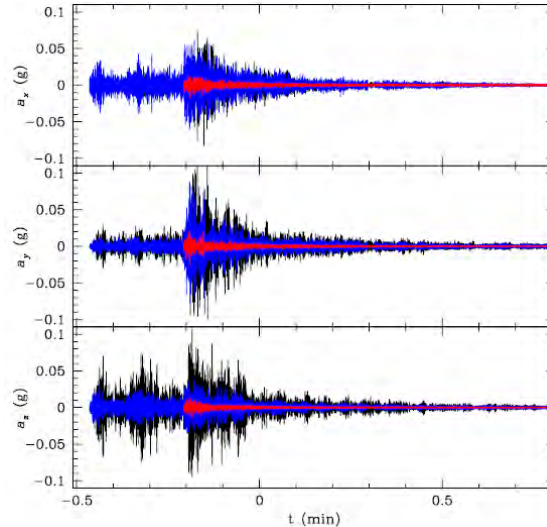


Figure 5 – Three-axis acceleration response of the Magellan Telescopes to a minor seismic event. The red shows the seismic input, and the blue and black show two locations exhibiting significant dynamic amplification.

In 2010, a magnitude 8.8 M_w earthquake occurred approximately 1.9 miles off the coast of Chile in the Maule Region. It was the fifth largest earthquake ever to be recorded by a seismograph and GPS measurements showed LCO moved 3 cm to the west [6]. The time history of the seismic event was processed to give expected responses at LCO as part of the Site-specific Seismic Hazard Report (Figure 6) [2]. This processed acceleration time history was used as the input for all analyses.

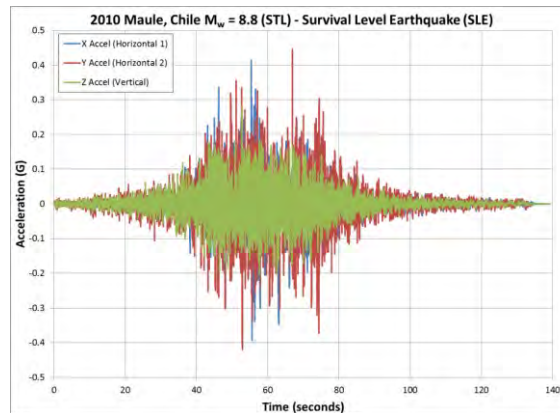


Figure 6 – Three-axis survival level earthquake acceleration expected at LCO. Used as inputs for seismic analysis of Magellan Telescope.

2.3 Damping

In a mode based analysis, damping would be expressed in terms of percent of critical damping based on frequency or modes. For large steel structures with bolted joints such as the Magellan Telescopes, this value may range from 2% up to 5% if some additional damping due to minor yielding is desired. This analysis assumes that no yielding occurs, and thus 2% critical damping is used. For a transient analysis, however, percent of critical damping cannot be specified directly. Rayleigh damping is used for implicit dynamic analyses

$$\zeta = \frac{\alpha}{2\omega} + \frac{\beta\omega}{2} \quad (1)$$

where ζ is percent critical damping, α and β are damping factors, and ω is the frequency of the mode. α and β are used to construct the damping matrix (C) according to

$$C = \alpha M + \beta K \quad (2)$$

where M is the mass matrix and K is the stiffness matrix. Preliminary analysis of the structure (Section 3.1) indicated that the first lateral/rocking mode was 7.8 Hz and the first vertical mode was 13.6 Hz. Using these modes for the Rayleigh equation, and 2% critical damping, $\alpha = 1.25$ and $\beta = 2.97 \text{ E } -4$. This gives the Rayleigh damping shown in Figure 7. Constant 2% critical damping is also shown for reference. Although this creates ever increasing damping for higher frequency content, the damping is correct for the primary modes where most of the structural response is concerned.

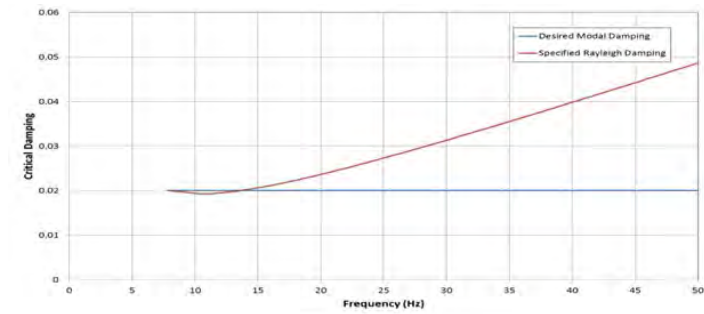


Figure 7 – Rayleigh damping assuming $\alpha=1.25$, $\beta=2.97\text{E}-4$, $\omega_1 = 7.8$ Hz, and $\omega_2 = 13.6$ Hz.

Connectors were given exactly 2% critical damping, since it can be specified directly using viscous damping according to

$$c = 2m\omega\zeta \quad (3)$$

where c is viscous damping and m is mass. The M1 mirror supports were given 10% critical damping, which is a conservative estimate for wire rope isolators based on prior experience and testing. The mass and stiffness of the M1 mirror and support system were used in the calculation of their respective damping.

2.4 Analysis and boundary conditions

A nonlinear implicit dynamic analysis of each configuration was performed using Abaqus/Standard 6.14-3 [1]. The three-axis acceleration time history was applied to the free end of the soil connector attached to the pier (Figure 6). The time history was trimmed to approximately 90s to reduce simulation time; peak acceleration and dynamic superposition are accounted for by including all accelerations below 90s. Forces, displacements, accelerations, and stress were monitored for the telescope structure. The analysis consists of three steps:

1. Preload the secondary vanes and FourStar Nasmyth Instrument Rotator offloading beam (Configuration 1 only)
2. Apply gravity
3. Apply three-axis acceleration time history

For all steps, the free end of the soil connector was fully constrained (except during the transient step when all 3 translations are released) and the non-linear geometry option was activated to allow large displacement calculations to remain valid. Three models were analyzed:

1. Configuration 1 at zenith (Z0)
2. Configuration 2 at zenith (Z0)
3. Configuration 2 at 60° off zenith (Z60)

3 RESULTS

Results during the dynamic step were sampled every 0.004 s according to the equation

$$S = \frac{1}{5 \cdot \omega} \quad (4)$$

where ω is the highest natural frequency of interest (50 Hz in this case, the maximum frequency content in the earthquake time history provided by URS - Figure 6 [2]). Acceleration results are only shown from 25-90s since accelerations below 25s are low. Stress results were enveloped over the entire analysis so that one contour could be displayed showing the peak stress in all elements. Therefore, stress results displayed below are not necessarily occurring simultaneously, but represent the worst stress experienced by all elements.

3.1 Preliminary results and model checks

Some preliminary analyses were performed to check that the model was performing as expected. These included linear modal analysis (all of the hydrostatic bearings had an equivalent linear stiffness) and static analysis of 1G gravity loads. The linear modal response predicted the primary lateral/rocking mode at approximately 7.8 Hz and the primary vertical mode at 13.6 Hz for Configuration 1 (Figure 8). *In situ* measurements showed the primary lateral/rocking mode within the same range as predicted.

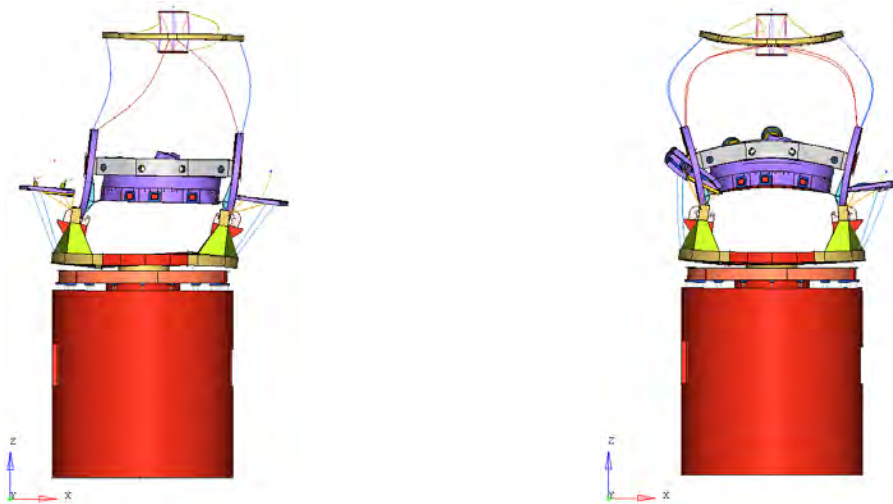


Figure 8 – Mode shape of primary lateral/rocking mode (left, 7.8Hz) and primary vertical mode (right, 13.6 Hz).

Linear modal analysis for Configuration 2 showed a similar frequency for the primary lateral/rocking and vertical modes, and a slight drop (~4%) in the primary lateral/rocking mode for Configuration 2 Z60. The primary lateral/rocking mode dropped slightly because the ribs in the altitude disks providing much of the stiffness are no longer oriented orthogonal to the mode direction. Even though slightly different frequencies were calculated for the different configurations, the same damping was maintained to more readily compare results.

Figure 9 shows the deformation of each model under 1G. In all three models the M1 mirror experiences the largest deformation under 1G with Configuration 1 showing the most extreme deformation since the M1 mirror static supports are the most compliant in this configuration.

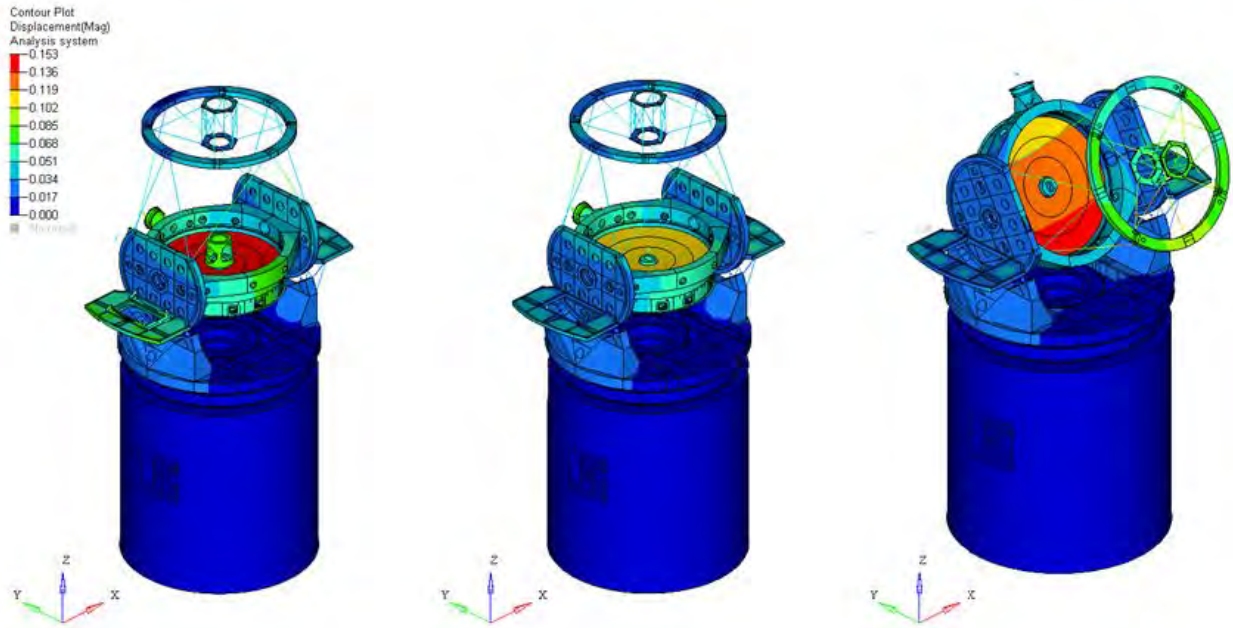


Figure 9 – Deformation of FEMs under 1G static load. Configuration 1 Z0 (left), Configuration 2 Z0 (middle), and Configuration 2 Z60 (right). Units are in inches. Gravity is applied in the Z direction for all three models.

3.2 Acceleration results

A summary of the acceleration results are shown here, highlighting key areas and interesting results. For components represented with a concentrated mass, the acceleration results are of that specific element. For components represented with a more explicit mesh (M1 mirror), the accelerations shown are the peak accelerations in the component in each direction and may not necessarily be occurring at the same location. The peak acceleration is reported at each location to remain conservative for future component level and instrument analysis. For a future static analysis, a 1G load would be added to the reported values in the $-Z$ direction; adding a constant 1G offset to the transient Z results is not appropriate. Results for Configuration 2 Z60 are presented in the global coordinate system so that gravity aligns with Z accelerations.

Table 3 – Peak acceleration summary.

Config. 1 Component	Location	Config 1 Z0 (g)						Config. 2 Component	Location	Config 2 Z0 (g)						Config 2 Z60 (g)					
		X		Y		Z				X		Y		Z		X		Y		Z	
		Pos.	Neg.	Pos.	Neg.	Pos.	Neg.			Pos.	Neg.	Pos.	Neg.	Pos.	Neg.	Pos.	Neg.	Pos.	Neg.	Pos.	Neg.
Input	Input	0.41	-0.39	0.44	-0.42	0.27	-0.20	Input	Input	0.41	-0.39	0.44	-0.42	0.27	-0.20	0.41	-0.39	0.44	-0.42	0.27	-0.20
M1	Primary	0.79	-0.80	0.74	-0.87	0.90	-0.66	M1	Primary	1.44	-1.40	1.08	-1.25	2.01	-1.86	1.36	-1.41	1.79	-1.71	1.00	-1.03
F11	Secondary	1.36	-1.53	1.34	-1.10	1.75	-1.84	AO	Secondary	1.57	-1.45	1.36	-1.44	2.24	-2.32	1.48	-1.29	1.50	-1.75	2.40	-1.74
M3	Tertiary	0.79	-0.86	0.79	-1.10	0.85	-0.85	M3	Tertiary	0.89	-0.97	0.76	-0.94	0.88	-0.59	0.96	-1.05	0.75	-1.38	0.97	-0.67
IMACS	West Nasmyth	0.87	-1.02	0.92	-0.90	0.66	-0.62	MIKE	East Nasmyth	1.92	-2.24	1.64	-2.07	1.18	-0.77	2.15	-1.95	1.66	-2.11	1.90	-1.30
FOURSTAR	East NIR	0.86	-0.83	0.73	-0.85	1.65	-0.84	LDSS3 NIR	West NIR	0.96	-0.96	0.71	-0.89	0.97	-0.56	0.85	-0.92	1.18	-0.85	1.61	-0.87
FIRE	FPIR	1.31	-1.30	1.08	-1.20	1.26	-1.30	LDSS3 FPIR	FPIR	1.12	-1.01	0.80	-1.10	1.55	-1.29	1.40	-1.30	2.28	-3.26	1.13	-1.45

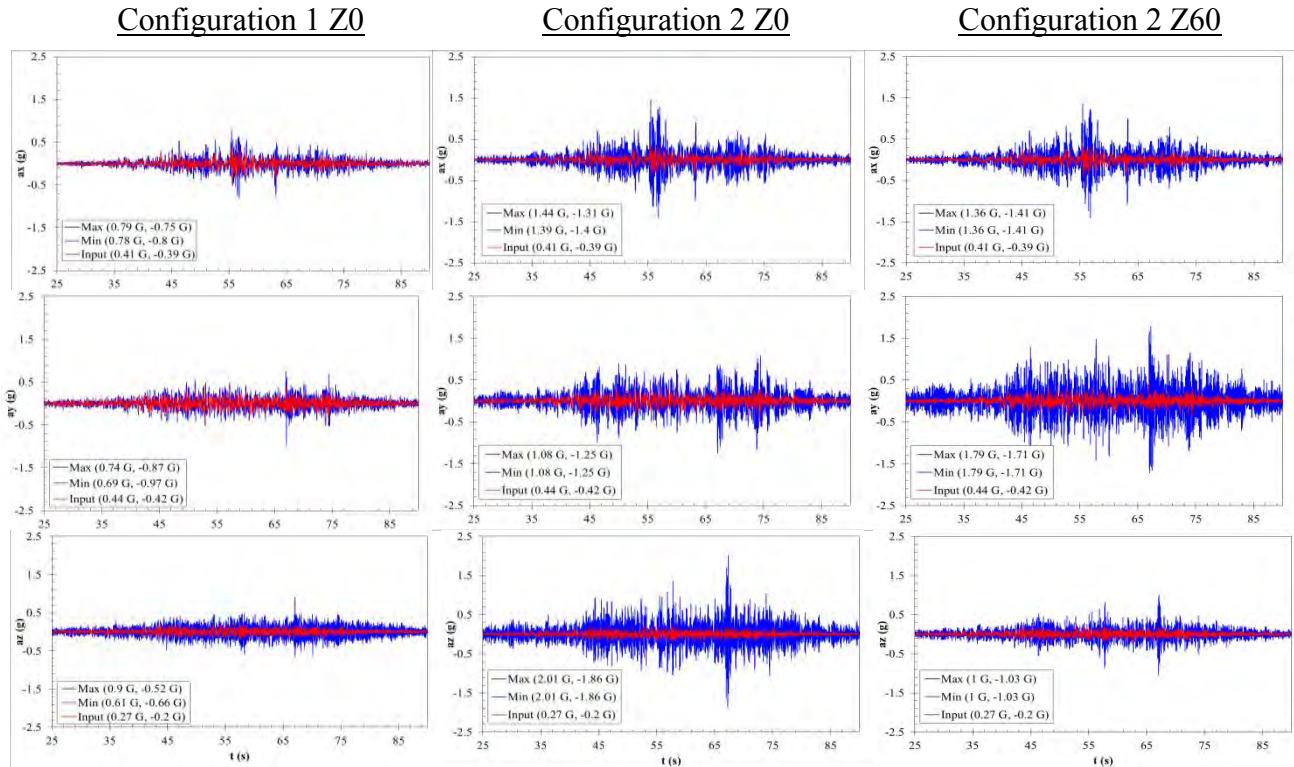


Figure 10 – M1 mirror peak accelerations.

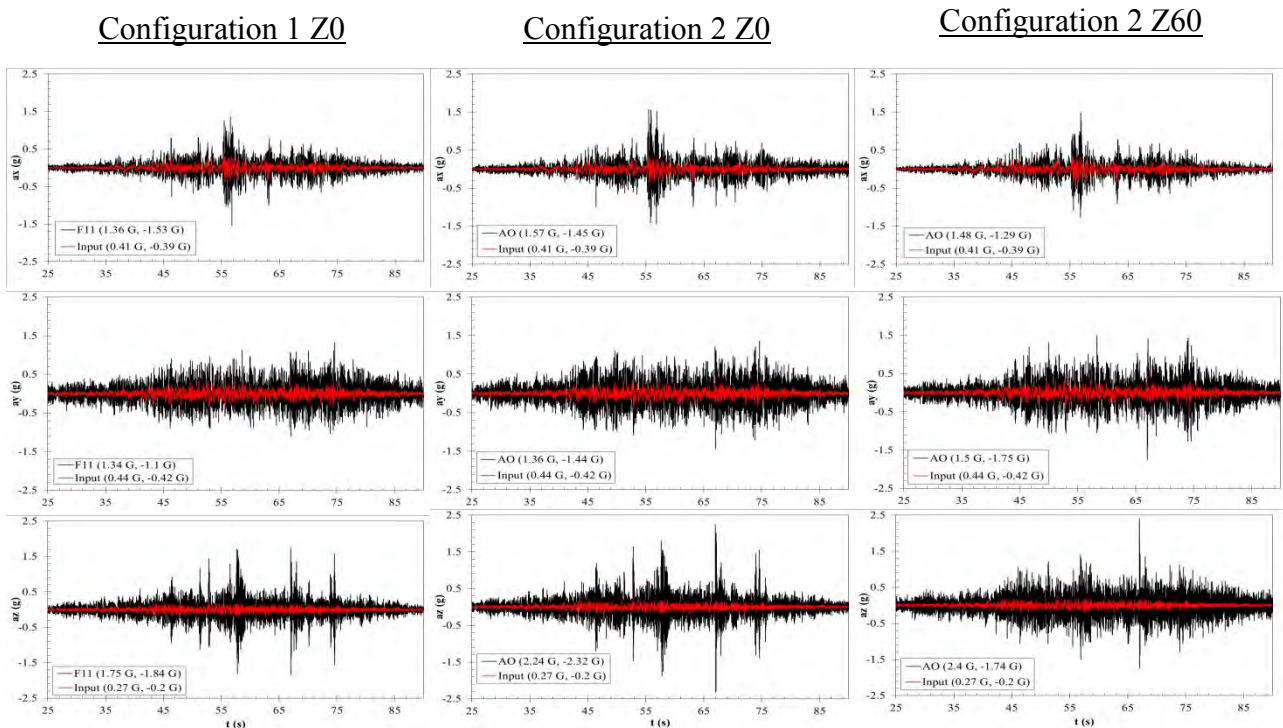


Figure 11 – Secondary peak accelerations. Configuration 1 uses an f/11 at the secondary. Configuration 2 is using an adaptive optic.

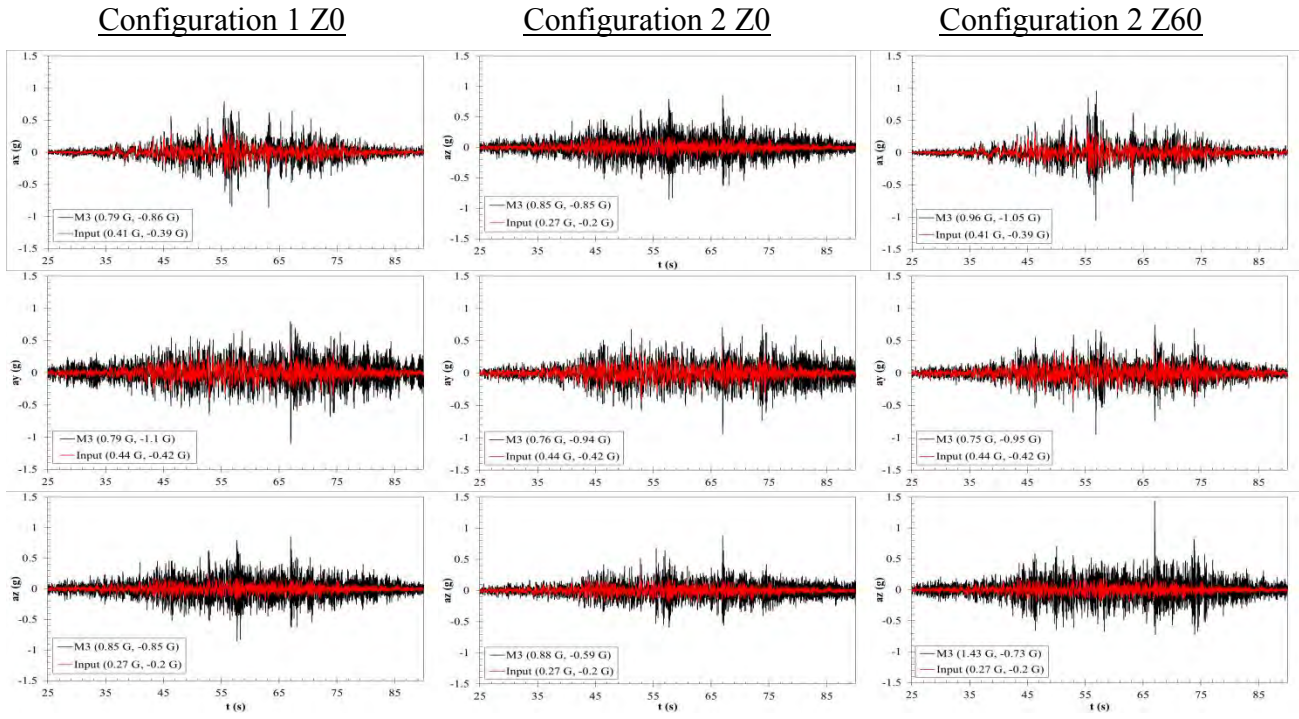


Figure 12 – M3 mirror peak accelerations.

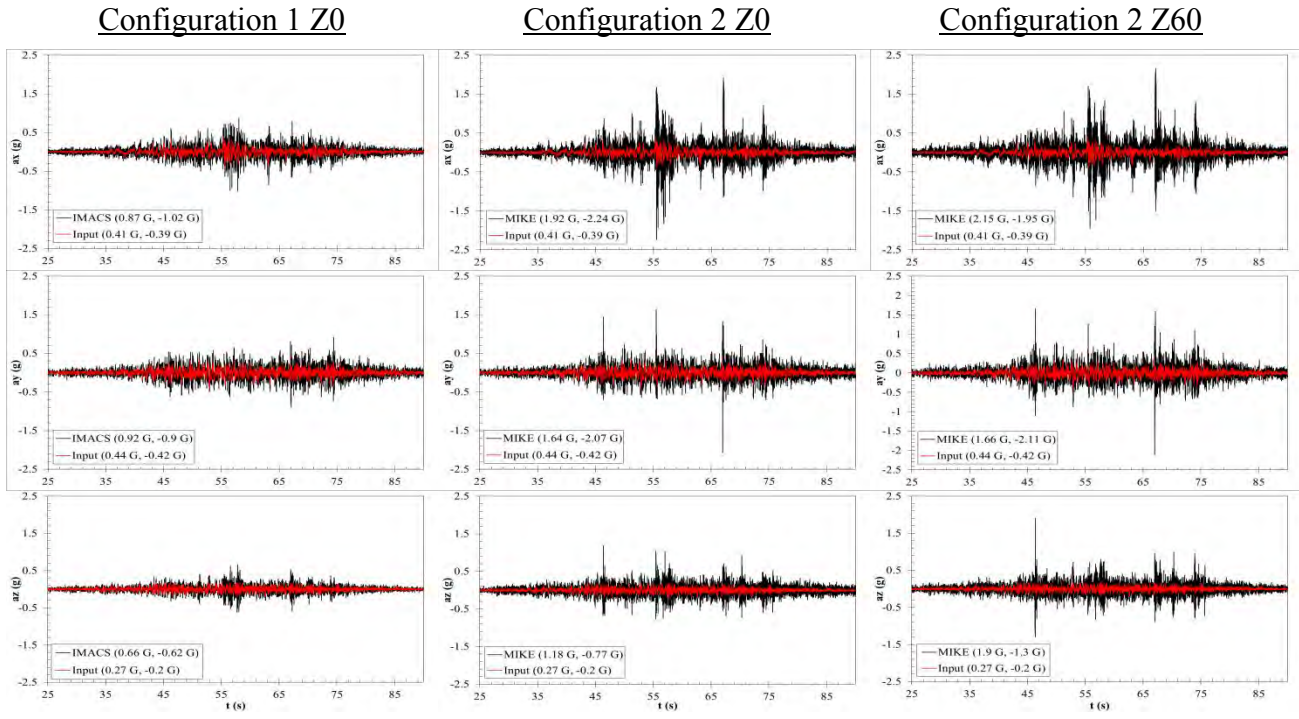


Figure 13 – Nasmyth instruments peak accelerations. Configuration 1 is IMACS on West Nasmyth and Configuration 2 is MIKE on East Nasmyth.

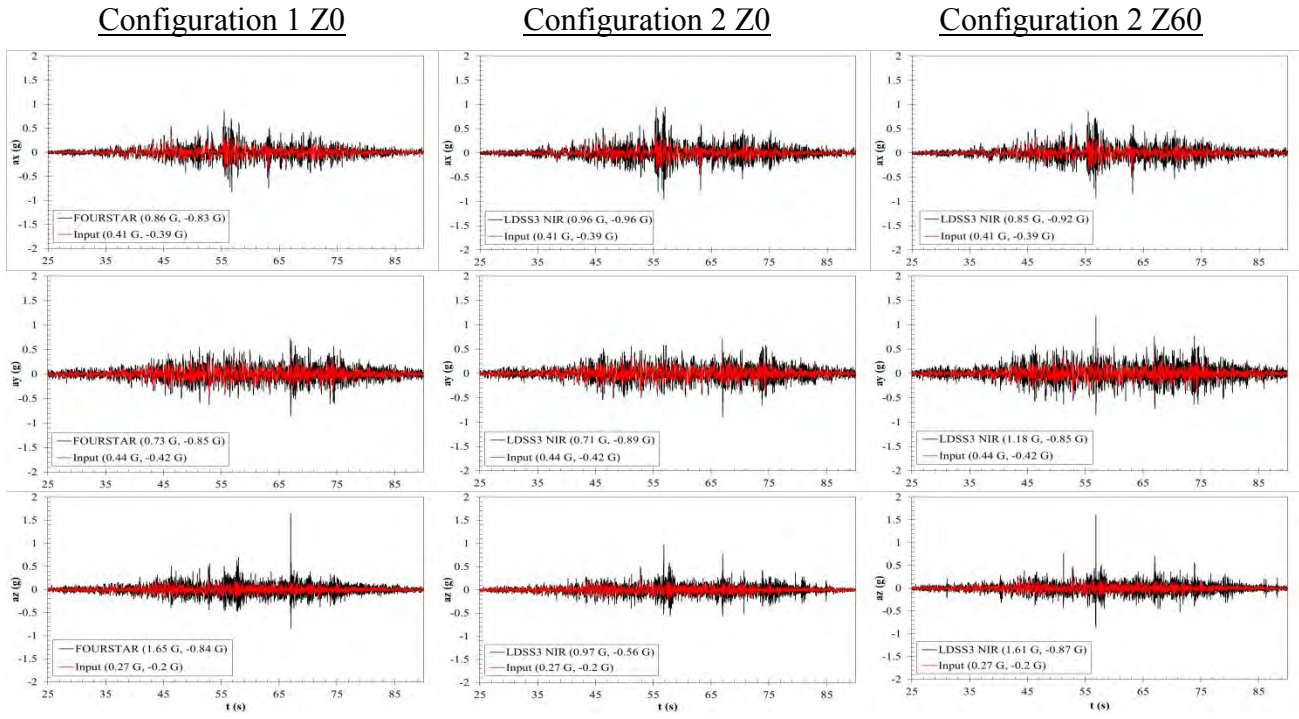


Figure 14 – NIR instruments peak acceleration. Configuration 1 is FourStar on East NIR and Configuration 2 is LDSS3 on West NIR.

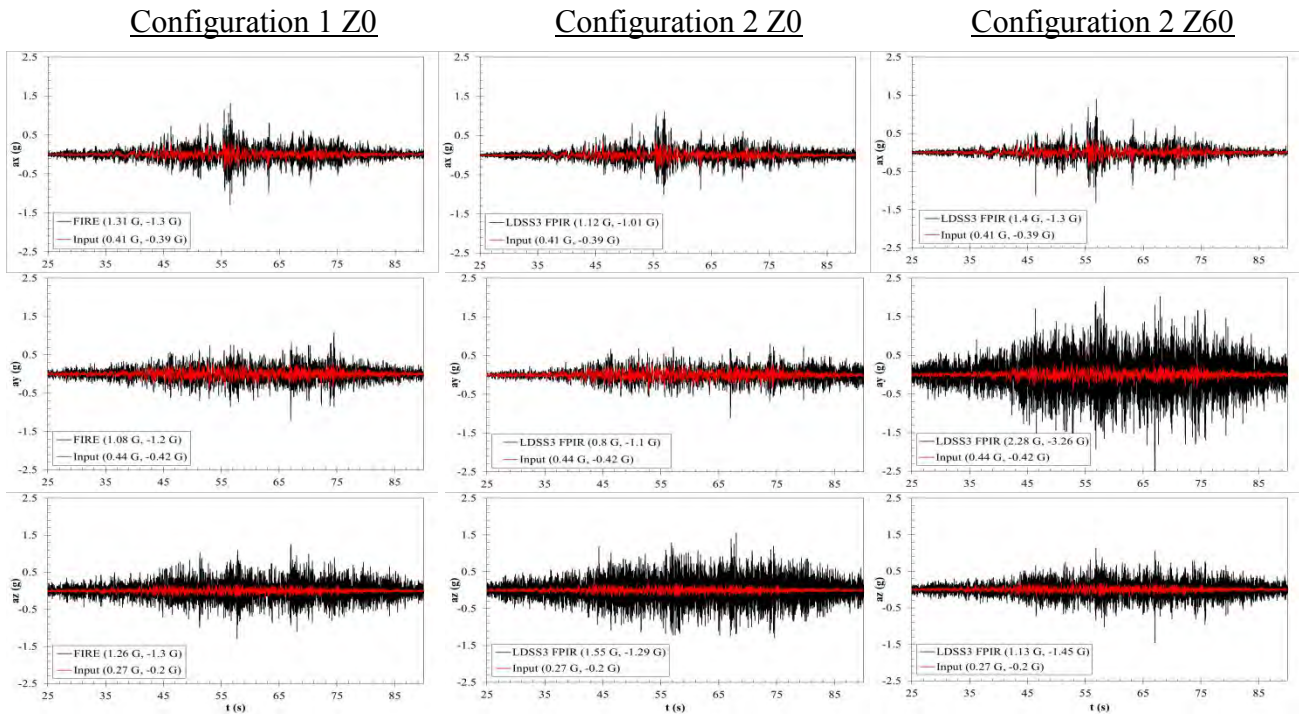


Figure 15 – FPIR instruments peak acceleration. Configuration 1 is FIRE and Configuration 2 is LDSS3.

3.3 M1 mirror displacements

Displacements of the M1 mirror are shown in axial and lateral directions. Axial is along the optical axis and lateral are the two orthogonal directions (Figure 16 shows these directions on Configuration 2 Z60 but they are similar for all

configurations). Peak displacements are shown in Table 4. Displacements are relative to M1 cell and are enveloped over the entire time history. Peak displacements may not be occurring simultaneously or in the same location.

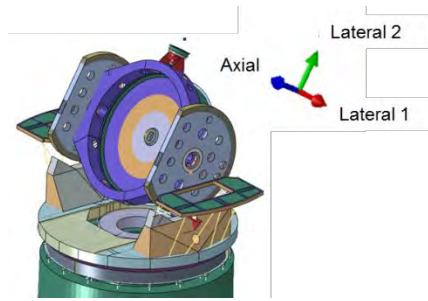


Figure 16 – Axial and lateral directions for M1 mirror displacements shown here on Configuration 2 Z60

Table 4 – M1 mirror displacements

Component	Configuration 1 Z0		Configuration 2 Z0		Configuration 2 Z60	
	Max	Min	Max	Min	Max	Min
Lateral 1 (in)	0.30	-0.27	0.13	-0.15	0.15	-0.13
Lateral 2 (in)	0.21	-0.22	0.08	-0.13	0.02	-0.14
Axial (in)	0.13	-0.32	0.11	-0.20	0.13	-0.13

3.4 Stress results

Stress is shown in all components using A36 steel (a majority of the structure) and the adjustable anchors only. Stress was investigated elsewhere in the structure, but values were low and the results were omitted from this report.

3.4.1 A36 stress results

Enveloped stress results for components using A36 steel are shown below. Yield stress is 36.3 ksi and ultimate stress is 58 ksi.

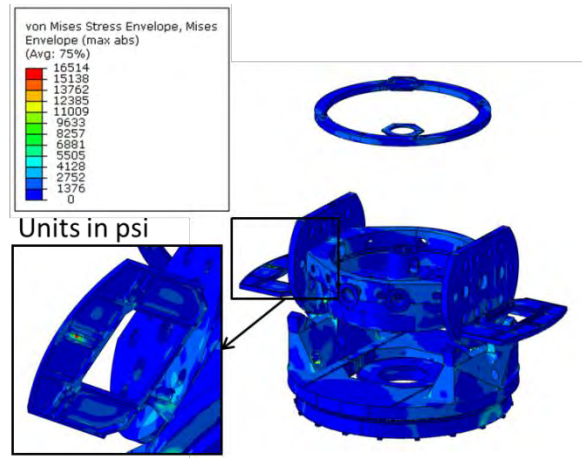


Figure 17 – Stress envelope results for A36 steel in Configuration 1 Z0. Peak stress is 16.5 ksi and is below the Fourstar offload beam. Yield stress is 36.3 ksi and ultimate stress is 58 ksi.

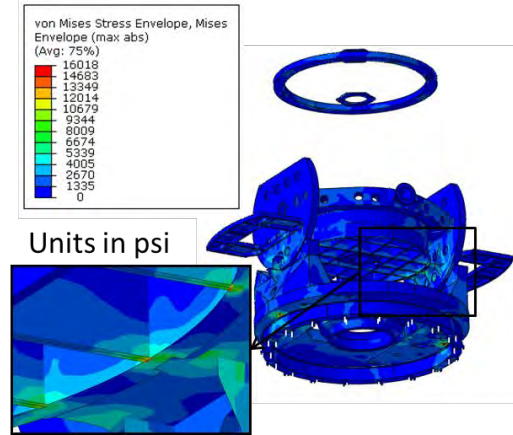


Figure 18 – Stress envelope results for A36 steel in Configuration 2 Z0. Peak stress is 16.0 ksi and is on the M1 cell. Yield stress is 36.3 ksi and ultimate stress is 58 ksi.

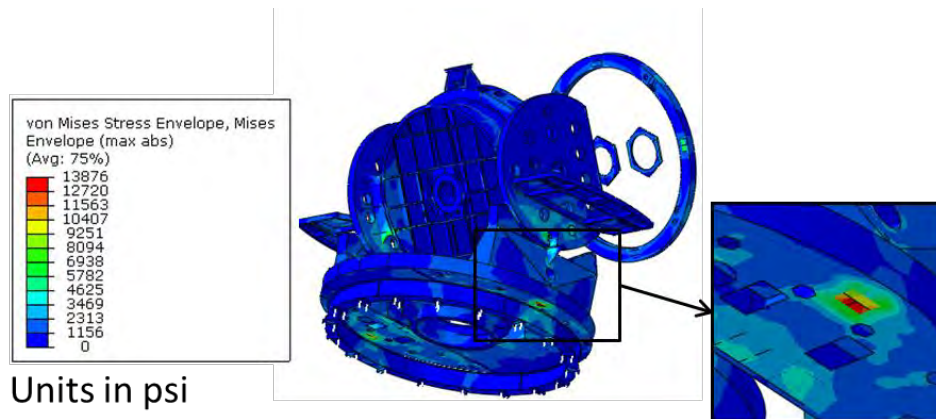


Figure 19 – Stress envelope results for A36 steel in Configuration 2 Z60. Peak stress is 13.9 ksi and is above an azimuth vertical bearing on the azimuth disk. Yield stress is 36.3 ksi and ultimate stress is 58 ksi.

3.4.2 Beam stress results

Stress in components represented with beam elements (vanes, trusses, and adjustable anchors) was calculated using enveloped beam forces and moments. Stresses shown may not be occurring simultaneously or in the same location but are a conservative representation of stress.

The adjustable anchors are a ring of adjustable fasteners connecting the ring beam to the pier; they are used to level the telescope. Figure 20 shows a picture and the FEM representation of one of the adjustable anchors. Stress is only reported in the small unsupported length.

Table 5 lists the peak stresses for each configuration.

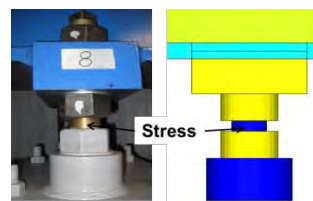


Figure 20 – Adjustable anchors modeled with different diameter beam elements. Stress reported in small unsupported length only.

Table 5 – Adjustable anchors stress summary. Yield stress is 124 ksi (4140 heat treated steel).

Component	Configuration 1 Z0	Configuration 2 Z0	Configuration 2 Z60
Axial Stress (ksi)	-16.68	-16.02	-15.65
Shear Stress (ksi)	2.52	2.65	2.51
Bending Stress 1 (ksi)	60.98	61.93	62.93
Bending Stress 2 (ksi)	109.56	106.34	106.37
Peak Combined (Axial + Bending)	126.24	122.36	122.02

3.5 Vane preload results

Figure 21 shows the orientation for radial and axial loads on the vane ends. Figure 22 -

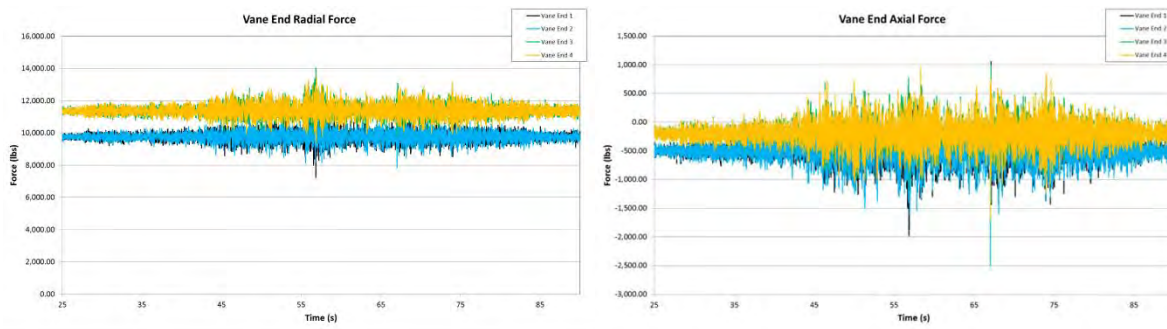


Figure 24 show the radial and axial preloads for each configuration. Table 6 lists the peak radial forces seen in each vane end for each configuration, and Table 7 lists the peak axial forces.

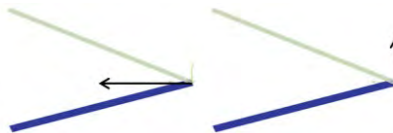


Figure 21 – Radial and axial load on the vane ends. Radial loads point from the secondary ring towards the secondary cage. Axial loads point orthogonal to this direction, parallel to the optical axis.

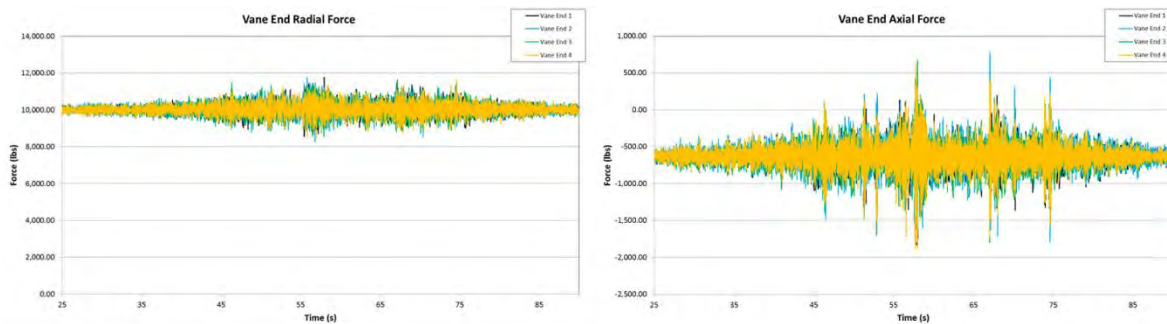


Figure 22 – Radial and axial loads in the vane ends for Configuration 1 Z0. Radial loads oscillate about the preload value of 10,000 lbs and axial loads oscillate about an initial value of -600 lbs.

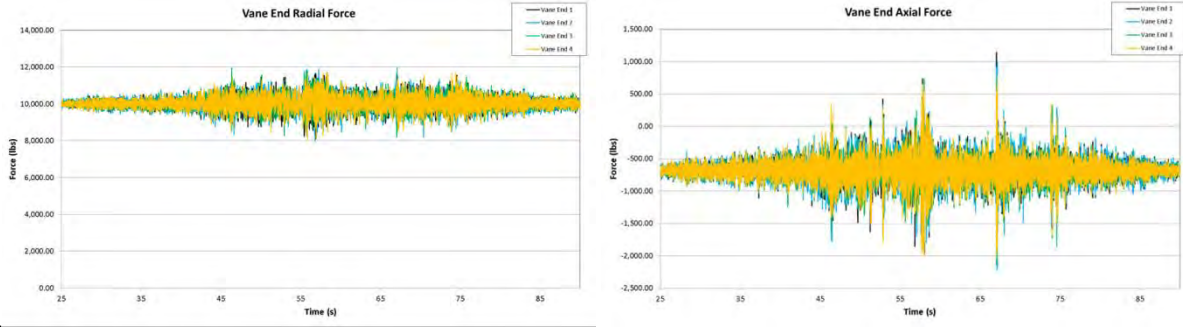


Figure 23 – Radial and axial loads in the vane ends for Configuration 2 Z0. Radial loads oscillate about the preload value of 10,000 lbs and axial loads oscillate about an initial value of -600 lbs.

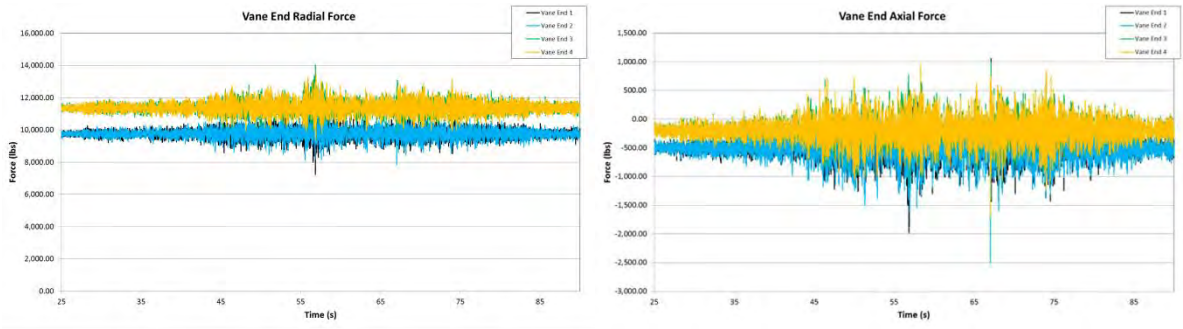


Figure 24 – Radial and axial loads in the vane ends for Configuration 2 Z60. Vane ends 1 and 2 are below the secondary cage in this configuration and oscillate about an initial radial preload of 9,700 lb and an initial axial preload of -500 lbs. Vane ends 3 and 4 are above the secondary cage in this configuration and oscillate about an initial radial preload of 11,300 lbs and an initial axial preload of -300 lbs.

Table 6 – Peak radial forces for each vane end in each configuration.

Vane End	Configuration 1 Z0		Configuration 2 Z0		Configuration 2 Z60	
	Max	Min	Max	Min	Max	Min
1	11,774	8,558	11,660	8,064	11,986	7,230
2	11,764	8,265	11,960	7,970	11,775	7,827
3	11,641	8,530	11,942	8,214	14,034	9,782
4	11,642	8,443	11,692	8,020	13,427	9,398

Table 7 – Peak axial forces for each vane end in each configuration.

Vane End	Configuration 1 Z0		Configuration 2 Z0		Configuration 2 Z60	
	Max	Min	Max	Min	Max	Min
1	724	-1,827	1,146	-2,065	1,057	-2,407
2	777	-1,790	980	-2,214	736	-2,501
3	676	-1,800	730	-2,135	994	-1,706
4	636	-1,877	775	-2,047	952	-1,685

3.6 Hydrostatic bearing results

Force and displacement were tracked in each hydrostatic bearing. Figure 25 and Figure 26 show representative plots of forces and displacements respectively, of the Large Azimuth Vertical bearings for Configuration 1. Figure 27 and Figure 28 show similar plots for the OSS Radial bearings for Configuration 1.

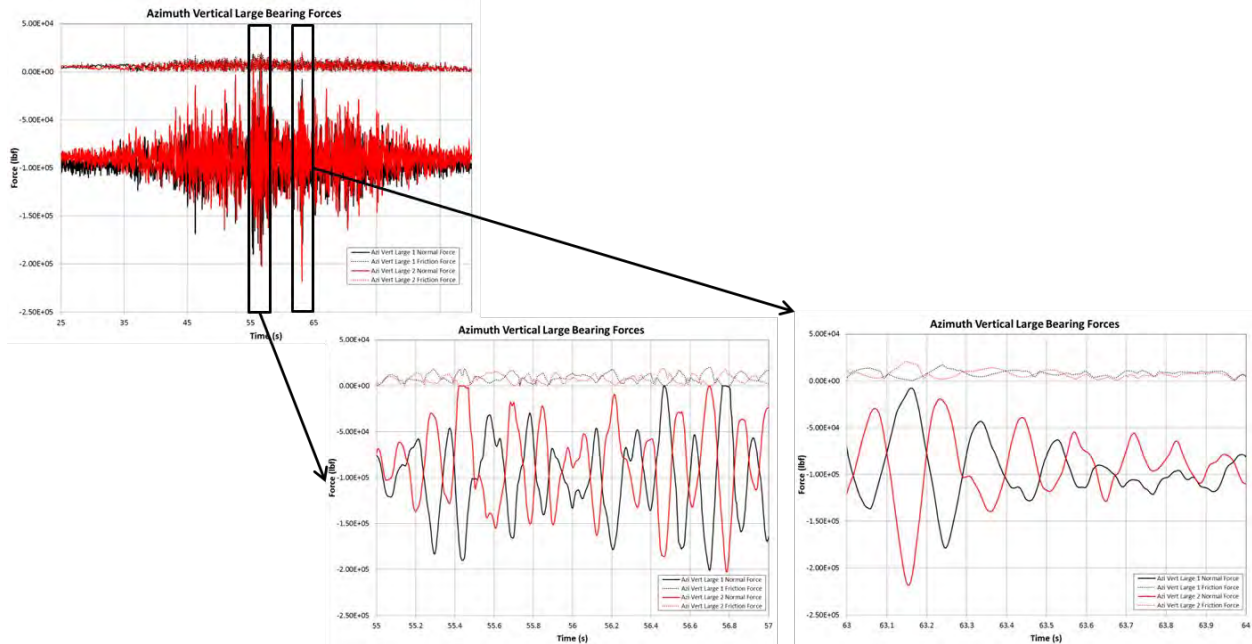


Figure 25 – Normal and friction forces in large azimuth vertical bearings for Configuration 1 Z0. Large azimuth vertical bearings are on either side of the azimuth disk underneath the elevation discs.

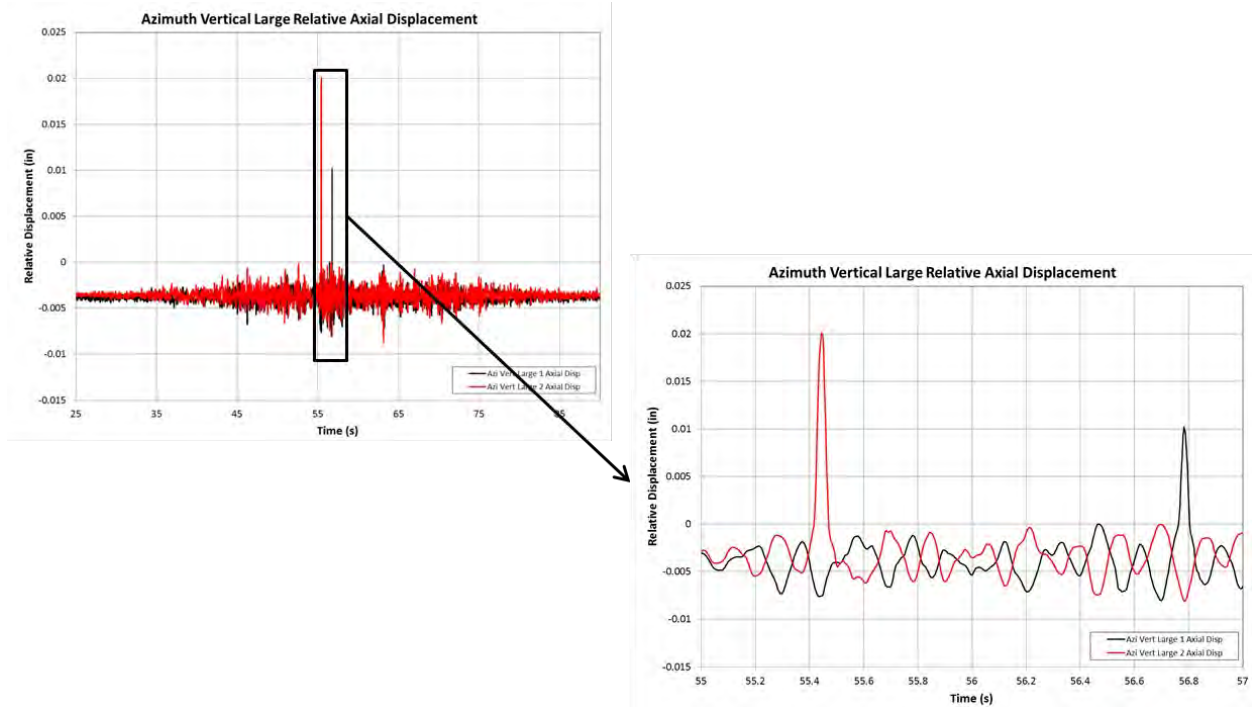


Figure 26 – Axial displacements of large azimuth vertical bearings for Configuration 1 Z0. Large azimuth vertical bearings are on either side of the azimuth disk underneath the elevation discs.

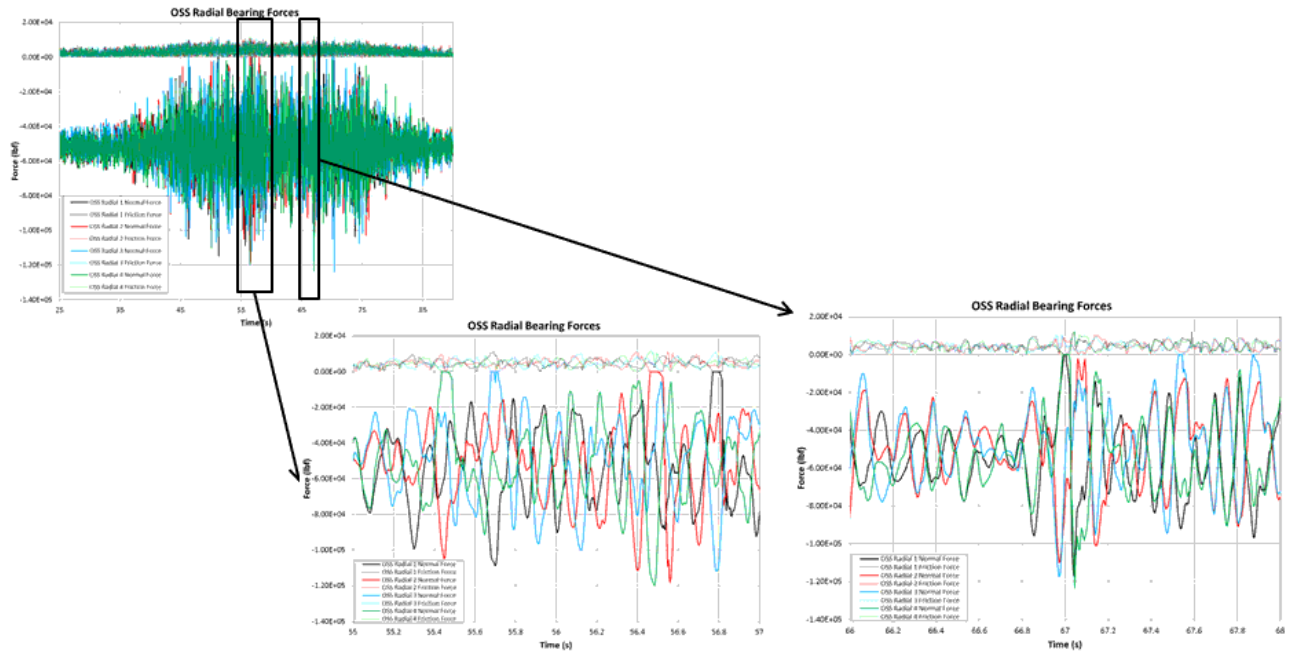


Figure 27 – Normal and friction forces in OSS radial bearings for Configuration 1 Z0. OSS radial bearings are between the elevation discs and the azimuth pillow blocks.

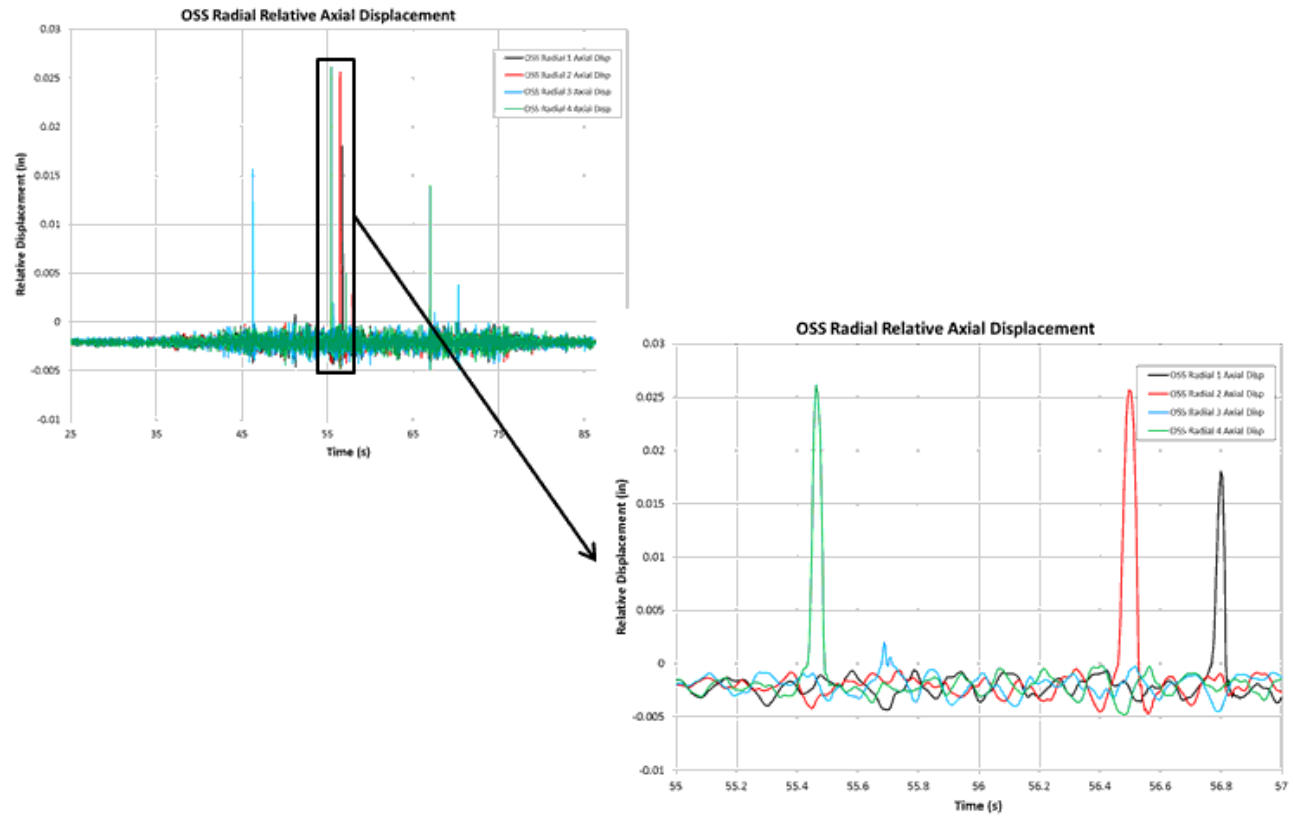


Figure 28 – Axial displacement of OSS radial bearings for Configuration 1 Z0. OSS radial bearings are between the elevation discs and the azimuth pillow blocks.

Table 8 – Peak hydrostatic bearing axial lift off.

Bearing	Configuration 1 Z0	Configuration 2 Z0	Configuration 2 Z60
Azi Vert Large	0.020 in	0.037 in	0.038 in
Azi Vert Small	0.056 in	0.047 in	0.046 in
Azi Radial	0.038 in	0.045 in	0.040 in
OSS Lateral	0.027 in	0.027 in	0.030 in
OSS Radial	0.026 in	0.053 in	0.044 in

Table 9 – Peak hydrostatic bearing axial force.

Bearing	Configuration 1 Z0	Configuration 2 Z0	Configuration 2 Z60
Azi Vert Large	-218,301 lbf	-213,031 lbf	-213,674 lbf
Azi Vert Small	-97,216 lbf	-99,287 lbf	-100,842 lbf
Azi Radial	-174,911 lbf	-203,719 lbf	-188,892 lbf
OSS Lateral	-71,726 lbf	-85,485 lbf	-72,253 lbf
OSS Radial	-123,797 lbf	-135,969 lbf	-130,445 lbf

Table 10 – Peak hydrostatic bearing lateral friction force. The azimuth radial and OSS lateral hydrostatic bearings were not given friction.

Bearing	Configuration 1 Z0	Configuration 2 Z0	Configuration 2 Z60
Azi Vert Large	20,809 lbf	20,472 lbf	19,839 lbf
Azi Vert Small	9.722 lbf	15,430 lbf	13,802 lbf
Azi Radial	-	-	-
OSS Lateral	-	-	-
OSS Radial	12,348 lbf	19,680 lbf	24,973 lbf

4 DISCUSSION AND CONCLUSIONS

Significant dynamic amplification exists in the structure for all configurations. At most locations, peak accelerations occur at specific, consistent time points (just after 55 and 65 seconds). A closer investigation of the transient deformations and plotted results at these time points revealed that the lateral/bending mode was being excited. Not only did the deformations clearly show the motion, but a rough estimate of the frequency of results as these peak locations was calculated at approximately 8-9 Hz. The frequency is slightly different from the initial estimate of the lateral/bending mode since the initial model did not account for damping or nonlinearity.

The M1 mirror experiences consistently higher accelerations but smaller motions in Configuration 2 due to the stiffer static supports. The secondary mirror in Configuration 2 (AO) also experiences higher peak accelerations due to the increase in weight from the Configuration 1 secondary mirror (f/11; 1000 lbs vs 800 lbs). In all results for Configuration 2 Z0 and Z60, recall that accelerations are being reported in the global coordinate system for both models, which does not rotate with the OSS.

M3 accelerations are relatively similar for both configurations. Although Configuration 2 is slightly heavier (~2,700 lbs vs 2,000 lbs for the whole M3 assembly), it uses a different M3 turret and does not have an ADC.

MIKE and IMACS are compared even though they are on opposite Nasmyth platforms because they are similar heavy instruments. IMACS also has an attachment to the NIR, but it only carries load along the elevation axis. MIKE experiences significantly higher accelerations than IMACS even though IMACS is significantly heavier (7,700 lbs vs 1,300 lbs). This is because of the way MIKE and IMACS' attachment to the structure was modeled. The carriage and rollers were both modeled for IMACS, whereas MIKE was just rigidly attached to the Nasmyth platform with a kinematic coupling. This effectively isolated IMACS from some of the acceleration, but gives a more conservative estimate of accelerations that MIKE might experience in an SLE.

The NIR and FPIR instruments shown also have similar accelerations. The consistent dynamic amplification on the FPIR instruments in the Z direction (and Y for Z60) is due to the instruments being in the middle of the large unsupported

length of the center section, and further compounded by being cantilevered out on the FPIR. A similar, although less severe, result was observed on the adjacent location of the center section.

If any of these acceleration levels are to be used for future instrument design, the peak acceleration level should be applied statically in each global direction. A 1G vertical load would need to be added to all Z accelerations in a static analysis.

The M1 mirror shows significantly higher relative displacements for Configuration 1. Recall that Configuration 1 uses more compliant axial and lateral stiffness in the representation of the static supports.

Stress is low in the A36 steel for all configurations. The peak stress for all configurations is 16.5 ksi beneath the FourStar offload beam. It is likely conservatively high since the offload beam is connected to 1 node and not distributed over an area. In any case, this stress is well below the yield and ultimate allowables of 36.3 ksi and 58 ksi. Peak stress in the adjustable anchors is approaching (or slightly exceeding) the yield allowable. These stresses may not be occurring simultaneously or in the same anchor, but in the event of an SLE, the adjustable anchors should be inspected.

The vane end loads oscillate about their respective preload values and follow expected trends according to weight of the secondary and position of the telescope.

In Figure 25 and Figure 27, notice that the normal force never exceeds 0 lbf. This is most apparent on the left inlay in Figure 25 where there is a flat section of the curve just after 55.4s. These portions are where the hydrostatic bearings are experiencing lift off. Notice in Figure 26, the same azimuth vertical bearing (plotted in red) experiences positive axial displacement at the same time point. Also, note the change in slope of the displacement curve as the bearing lifts off. This signifies a change in velocity, and thus acceleration; the frequency of this event is 8.9 Hz, further pointing to this event as an effect of modal excitation of the structure. Similar results can be seen in Figure 28 and for all nonlinear bearings for all three configurations. The azimuth vertical bearings also exhibit a rocking effect at these time points (the force and displacement in either bearing oscillate out of phase from each other), which further corroborates a lateral mode being excited.

Axial lift off in all the bearings is low. This was one concern at the beginning of the analysis, that if lift off was high, some limiter would need to be retrofitted to constrain the telescope during a SLE.

A nonlinear transient survival level seismic finite element analysis of the Magellan telescopes showed that significant dynamic amplification occurs, and that modal excitation of the structure causes a nonlinear response and most of the peak responses. Some concern exists for stress in the adjustable anchors and displacement of the M1 mirror. Further analysis of the components and of the M1 mirror need to be performed before a comprehensive conclusion can be made to the durability of the Magellan Telescopes to an SLE.

REFERENCES

- [1] Dassault Systemes, "Abaqus/Standard 6.14-3," 2015.
- [2] URS Corporation, "Site-Specific Seismic Hazard Assessment of Proposed Giant Magellan Telescope Site, Las Campanas, Chile," 2011.
- [3] F. Kan, "Foundation Stiffness for Seismic Analysis of Magellan Telescopes," Simpson, Gumpertz, & Herger, 2015.
- [4] Altair Engineering, Inc., "HyperMesh 13.0," 2015.
- [5] B. Cuerden, "Wire Rope Static Supports for the LBT Primary Mirror," Steward Observatory, University of Arizona, Tucson, 2001.
- [6] P. Palunas, "The structural response of the Magellan telescopes to earthquakes," 2012.